

# LAGRANGIAN COHERENT STRUCTURES IN VARIOUS MAP REPRESENTATIONS FOR APPLICATION TO MULTI-BODY GRAVITATIONAL REGIMES

**Cody R. Short\***

Purdue University, United States of America  
crshort@purdue.edu

**Kathleen C. Howell†**

Purdue University, United States of America  
howell@purdue.edu

The Finite-Time Lyapunov Exponent (FTLE) has been demonstrated as an effective metric for revealing distinct, bounded regions within a flow. The dynamical differential equations derived in multi-body gravitational environments model a flow that governs the motion of a spacecraft. Specific features emerge in an FTLE map, denoted Lagrangian Coherent Structures (LCS), that define the extent of regions that bound qualitatively different types of behavior. Consequently, LCS supply effective barriers to transport in a generic system, similar to the notion of invariant manifolds in autonomous systems. Moreover, in general, FTLE values supply information describing the relative sensitivity in the neighborhood of a trajectory. Here, different models and variable representations are used to generate maps of FTLE and the associated structures are applied to design and analysis within an astrodynamical context. Application of FTLE and LCS to transfers from LEO to the  $L_1$  region in the Earth-Moon system are presented and discussed. Additionally, an example of FTLE analysis to an ARTEMIS stationkeeping maneuver is presented.

## I. INTRODUCTION

While many methodologies can produce viable options for a given application, a more informed process often produces similar results for less effort. In spacecraft trajectory design, such simulations often lead to viable first-order solutions but, ultimately, can only yield information that is, at most, as accurate as the underlying model. The addition of factors to increase the accuracy of the model allows for more realistic solutions and, generally, a more representative and informative design space. However, such expanded insight is frequently offset by the cost of additional complexity necessitating appropriate tools for the analysis.

For astrodynamical design, it is sometimes more appropriate to complete an initial investigation in a model that incorporates the simultaneous gravitational influences of several bodies. For example, transfer design between the Earth and the Moon benefits from simulations that simultaneously incorporate the gravitational influence of both bodies on a spacecraft. Additionally, perturbations from the Sun are significant, and the associated impact can be observed by com-

parisons. In such scenarios, preliminary results are obtained by modeling in terms of a simplified three- or four-body system. However, these initial results eventually require transition to a more realistic model involving, at least, the ephemerides of the gravitating bodies in preparation for applications to actual missions.

Analysis in models of varying levels of fidelity allows access to additional insight, but some useful methodologies must be modified or replaced. To vary fidelity, it is convenient to employ analysis options that apply to both the simplified and more complex models. The formulations underlying the Finite-Time Lyapunov Exponent (FTLE) and Lagrangian Coherent Structures (LCS) are applicable in any model where the paths of neighboring trajectories can be simulated. In fact, these methods are particularly useful when only experimental results from advection are available (i.e., when no underlying model accurately predicts the fate of the particles in a flow, but the actual trajectories can be observed).

The focus of this analysis is a demonstration of the applicability and extensibility of FTLE/LCS concepts in various models and representations. Specific application to trajectory design in the Earth-Moon-Sun system illustrates the value of these techniques and validates the tools within a more realistic mission de-

---

\*PhD Student, School of Aeronautics and Astronautics

†Hsu Lo Professor of Aeronautical and Astronautical Engineering

sign context. Maps of FTLE values and the LCS that emerge offer an informative view of a particular system at a given time and require only the calculation of a fairly simple quantity.

The subsequent discussion is fairly straightforward. Background with regard to previous efforts and FTLE/LCS theory as well as the models that are employed in the investigation are summarized. Some comments with regard to mapping strategies are offered. The goal of this work is apparent in an application of the theory to trajectory design as well as an example of FTLE as an analysis tool.

## II. LCS FORMULATIONS

### II.I Previous Contributions

The concept underlying LCS, as well as the name itself, originate with George Haller<sup>1,2</sup> and Haller and Yuan.<sup>3</sup> Haller also offers specific criteria to distinguish between structures arising from different effects when identifying LCS.<sup>4</sup> Shadden et al.<sup>5</sup> rigorously establish the fundamental concept that LCS act as transport barriers in the flow by proving that the flux across LCS is negligible. Mathur et al.<sup>6</sup> develop an effective implementation strategy for extracting LCS, and the relevance of LCS methodology in  $n$ -dimensional motion is established by Lekien et al.<sup>7</sup> Variational techniques for computing LCS are explored in Haller<sup>8</sup> as well as Farazmand and Haller.<sup>9</sup> Incorporating geodesic theory into the framework of transport barriers establishes a criteria for the convergence of LCS, guiding the selection of the appropriate time interval for the numerical simulation to compute LCS.<sup>10</sup>

Given the well-established theoretical foundations, the popularity of LCS has quickly expanded and active research continues in multiple disciplines. Simultaneous activities in computer science and visualization are focused on more effective computation and extraction of LCS. Specifically, work by Garth et al.<sup>11</sup> features adaptive mesh refinement for the calculation of FTLE near the structures of interest that delivers an improvement in the time efficiency of various methods for computing LCS. Additional applications of LCS include flow structures in aeronautical weather data, transport in the oceans, computational fluid dynamics, and even human musculoskeletal biomechanics, blood circulation, and airway transport.<sup>12</sup>

The application of FTLE and LCS concepts to astrodynamics has received some attention as well. Anderson<sup>13</sup> discusses the application of FTLE over relatively short time spans, denoted by Anderson as the Local Lyapunov Exponent (LLE), to identify sensitive regions along a trajectory. Various authors, including Lara et al.,<sup>14</sup> Villac,<sup>15</sup> and Villac and Broschart,<sup>16</sup> all apply fast Lyapunov chaoticity indicators, a metric similar in form to FTLE, for preliminary spacecraft

trajectory design and stability analyses in multi-body environments. In an application more closely associated with this investigation, Gawlik et al.<sup>17</sup> examine LCS in the mixed position-velocity phase space of the planar elliptic restricted three-body problem. Additional efforts to apply FTLE/LCS in the three-body problem within the context of periape mappings are offered by Short, Howell and Tricoche.<sup>18</sup> Pérez et al.<sup>19</sup> also examine the detection of invariant manifolds from LCS in the circular restricted three-body problem.

### II.II Computing the FTLE

While different metrics are employed to identify LCS, the finite-time Lyapunov exponent is generally the most common, where relatively high values of the FTLE indicate LCS. The FTLE essentially measures the stretching between adjacent trajectories over a prescribed time interval. Mathematically, the calculation of the FTLE is fairly straightforward. The flow map,  $\phi_{t_0}^t(\bar{x})$ , represents the state of the system that has evolved to a final time  $t$  from an initial state  $\bar{x}$  at time  $t_0$ . The FTLE<sup>‡</sup> is computed as the largest normalized eigenvalue of  $\sqrt{\frac{d\phi_{t_0}^t(\bar{x})}{d\bar{x}_0}{}^\top \frac{d\phi_{t_0}^t(\bar{x})}{d\bar{x}_0}}$ , i.e., the matrix spectral norm of the Jacobian with respect to the initial variations (<sup>‡</sup> indicates the matrix transpose). The matrix product,  $\frac{d\phi_{t_0}^t(\bar{x})}{d\bar{x}_0}{}^\top \frac{d\phi_{t_0}^t(\bar{x})}{d\bar{x}_0}$ , is also denoted the Cauchy-Green (CG) strain tensor, and the separate matrix,  $\frac{d\phi_{t_0}^t(\bar{x})}{d\bar{x}_0}$ , is the State Transition Matrix (also termed the STM and represented by  $\Phi(t, t_0)$  in this analysis) evaluated along the arc at time  $t$ . If several adjacent, initial state vectors are separated by small perturbations and subsequently evolved for a prescribed time, the Jacobian is estimated as described by Shadden et al.<sup>5</sup> in two dimensions via finite differencing such as,

$$\left. \frac{d\phi_{t_0}^t(\bar{x})}{d\bar{x}_0} \right|_{(i,j)} = \begin{bmatrix} \frac{x_{i+1,j}(t) - x_{i-1,j}(t)}{x_{i+1,j}(t_0) - x_{i-1,j}(t_0)} & \frac{x_{i,j+1}(t) - x_{i,j-1}(t)}{y_{i,j+1}(t_0) - y_{i,j-1}(t_0)} \\ \frac{y_{i+1,j}(t) - y_{i-1,j}(t)}{x_{i+1,j}(t_0) - x_{i-1,j}(t_0)} & \frac{y_{i,j+1}(t) - y_{i,j-1}(t)}{y_{i,j+1}(t_0) - y_{i,j-1}(t_0)} \end{bmatrix} \quad [1]$$

where the indices  $i$  and  $j$  indicate relative initial perturbations in  $x$  and  $y$ , respectively. These initial perturbations are defined with a regular grid spacing, however, such a grid spacing is not required.

Various schemes exist for calculating the Jacobian as required for computing FTLE values, including numerical integration of the variational equations, direct calculation from a grid of points (as in Equation [1]) or through the use of an auxiliary grid as described by Farazmand and Haller.<sup>9</sup> Direct computation from a grid of points that covers the domain of the simulation allows for calculating FTLE in systems where varia-

<sup>‡</sup>Here *the FTLE* refers to the largest finite-time Lyapunov exponent, which is generally of principle interest in FTLE/LCS analysis. However, some consideration<sup>20</sup> is also given to the smallest FTLE in the literature.

tional equations are not available. Selecting an appropriate grid spacing facilitates the identification of LCS consistent with the order of the grid spacing. A mesh that is too fine may exclude some structures. However, an auxiliary grid that brackets each of the primary grid points increases the accuracy of the resulting Jacobian. A heterogeneous approach using both the primary grid as well as an auxiliary grid supplies the most desirable results at the cost of additional computation.

With an evaluated flow map and its associated derivative, the FTLE ( $\lambda$ ) is then computed. Thus, the expression for the FTLE is,

$$\lambda = \frac{1}{|T|} \ln \tilde{\lambda}_{\max} \left( \sqrt{\frac{d\phi_{t_0}^t(\bar{x})}{d\bar{x}_0} \frac{d\phi_{t_0}^t(\bar{x})}{d\bar{x}_0}^\top} \right), \quad [2]$$

with  $\tilde{\lambda}_{\max}()$  representing the operation that extracts the largest eigenvalue of the operand. The parameter  $T = t - t_0$  represents both the truncation time for the FTLE and a means of normalizing the FTLE value.

### II.III LCS as Ridges in FTLE Scalar Fields

In practice, an entire field of FTLE values is often computed and displayed on a map or section. In this way, comparisons of FTLE values across a relatively large area are possible. Specifically, regions characteristic of similar FTLE values are identified. A single individual region may appear markedly different, in terms of FTLE value, than other regions within the field. Bounding these regions are height ridges corresponding to relatively large FTLE values. Such ridges are defined as curves where the FTLE values are maximal with respect to the largest principle curvature. These ridge values are largest with respect to the sides of the ridge but not necessarily along the top of the ridge where they may be greater or less than neighboring ridge values. Height ridges, their significance and computation, are given greater treatment by Eberly et al.<sup>21</sup> These FTLE ridges represent Lagrangian coherent structures, and act as boundaries in the flow separating regions of fundamentally different qualitative behavior. In autonomous systems, the LCS correspond to invariant manifolds while, in time-dependent flows, the LCS evolve with the flow while continuing to bound distinct regions of behavior.

### II.IV LCS as Streamlines of CG Vector Fields

While the FTLE is a convenient and relatively well-behaved measure of the stretching between neighboring trajectories, it represents only part of the information available from the Cauchy–Green tensor. Other valuable information is accessible directly from the eigenvalues and eigenvectors of the tensor. In two-dimensional flows, Haller and Beron–Vera<sup>10</sup> establish various vector fields with their associated streamlines

that correspond to transport barriers or LCS. Haller and Beron–Vera elaborate on exploiting all of the eigenvalues, eigenvectors and composite eigenvalue–eigenvector fields to identify different types of structures. For example, the particular streamlines that correlate with hyperbolic LCS are available from the eigenvector field consistent with the smallest eigenvalue. The vector field associated with this smallest eigenvalue is a strain field and yields a particular type of streamline, i.e., those denoted as strainlines. The strainlines with the smallest point–wise geodesic deviation are identified as hyperbolic transport barriers. Moreover, a selected tolerance on the value of the geodesic deviation supplies a criterion to identify convergence of the LCS and to calibrate algorithms for detecting such structures.

## III. SYSTEM MODELS

The computation of the FTLE is not contingent on any assumptions in the derivation of the system differential equations, and, thus, can be applied for systems modeled with various levels of fidelity. Consequently, generating maps of FTLE in successively more complex models highlights the effects of individual contributions on the flow in the system. As examples, FTLE values in the Circular Restricted Three–Body Problem (CRP), a Restricted Four–Body Problem (4BP) and a Moon–Earth–Sun (MES) point mass ephemeris model are investigated. To generate a scenario to initiate the investigation, a simple Hohmann arc in the Two–Body Problem (2BP) is employed. The associated governing equations as well as other necessary considerations in each model are summarized in this section.

### III.I The Two–body Model

The equations of motion for a massless body (in this case, the spacecraft) under the influence of a central gravitational field are represented in a rotating frame. Directions are identified by unit vectors:  $\hat{r}$  radially outward from the central body to the spacecraft,  $\hat{\theta}$  oriented 90° with respect to  $\hat{r}$  in the orbit plane and  $\hat{h} = \hat{r} \times \hat{\theta}$  consistent with the orbital angular momentum. The equations are expressed as two second–order coupled nonlinear differential equations,

$$\ddot{r} = r\dot{\theta}^2 - \frac{\mu_{2b}}{r^2}, \quad [3]$$

$$\ddot{\theta} = -\frac{2\dot{r}\dot{\theta}}{r}, \quad [4]$$

where  $r$  is the distance of the spacecraft from the central body in the  $\hat{r}$  direction,  $\dot{\theta}$  is the angular velocity of the rotating frame with respect to an inertial frame and  $\mu_{2b}$  is the central body gravitational parameter.

Despite the nonlinear, coupled nature of the equations, closed–form analytical solutions exist in the form

of well-known conic solutions. However, in this investigation, Equations [3] and [4] are converted to a system of four first-order nonlinear differential equations suitable for numerical integration for convenience and consistency when comparing between models.

### III.II The Restricted Three-body Model

Space environments of interest can involve multiple gravity fields, thus it is often necessary to incorporate as many of these gravity fields as possible into the governing models to ensure accurate simulation and to capture the essential features of the dynamical interactions. Models involving more than two bodies, however, offer no analytical solutions, and introduce additional complexities, which may be small but significant. Formulating the problem in terms of three bodies produces a model sufficiently complex to reveal many important characteristics while remaining tractable. However, even the general three-body problem possesses no closed-form solution.<sup>22</sup> Thus, additional simplifications, such as those consistent with the CRP, offer significant insight. The CRP incorporates only the effects of the masses of the two larger primaries (for example, the Earth and the Moon as they evolve on a mutual circular orbit) on a third, much smaller mass, such as a spacecraft.

Beyond this general description, a more careful mathematical definition for the CRP is important. The three bodies that appear in the model are designated as  $P_1$ ,  $P_2$ , and  $P_3$ —the body of interest. Position variables,  $x$ ,  $y$ , and  $z$  describe the position of the third body with respect to the barycenter of the primary system, which also serves as the origin of the rotating and inertial reference frames. The system mass parameter is represented by  $\mu = \frac{m_2}{m_1+m_2}$ , a function of the masses of the primary bodies. Additionally, distances between the third body and the two primaries are denoted  $r_{i3}$ . Specifically, in a coordinate frame that rotates coincident with the circular motion of the primaries, a system of differential equations that describes the motion of the third body incorporates the potential function,

$$U^* = \frac{1-\mu}{r_{13}} + \frac{\mu}{r_{23}} + \frac{1}{2}(x^2 + y^2), \quad [5]$$

and is written,

$$\ddot{x} = \frac{\partial U^*}{\partial x} + 2\dot{y}, \quad [6a]$$

$$\ddot{y} = \frac{\partial U^*}{\partial y} - 2\dot{x}, \quad [6b]$$

$$\ddot{z} = \frac{\partial U^*}{\partial z}, \quad [6c]$$

where the first derivatives in  $x$  and  $y$  appear as a result of Coriolis acceleration.

The equations of motion in the restricted problem<sup>§</sup> are consistent with Szebeheley<sup>23</sup> where they admit a single integral of the motion. This integral is termed the Jacobi integral and is represented as  $C$  in this analysis,

$$C = 2U^* - v^2, \quad [7]$$

where  $v^2 = \dot{x}^2 + \dot{y}^2 + \dot{z}^2$ , that is, the square of the magnitude of the relative velocity. This integral allows for a reduction of order in the problem, and frequently plays an important role in the definition of maps. The Jacobi integral reveals boundaries on the motion of the third body in the restricted problem. These boundaries are defined when the velocity in Equation [7] is zero, separating regions of real and imaginary velocities. An example of the Jacobi limiting boundaries, or Zero Velocity Curves (ZVC) in the  $x$ - $y$  plane, is depicted in Fig. 1 along with the two libration points near the second primary (in this case, Saturn at 50× scale in the Sun-Saturn system). These types of boundaries on the motion are intimately associated with the definitions of the maps employed here.

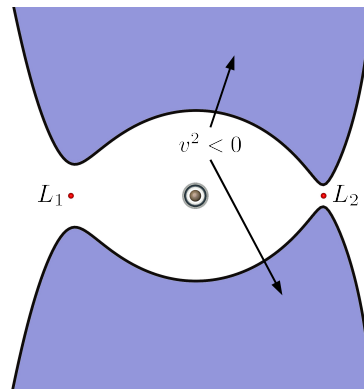


Fig. 1: Zero Velocity Curves in the  $P_2$  Region

The restricted problem represents a model of sufficient complexity to exhibit regions of both chaotic and relatively ordered behavior. Generally, the focus of the analysis is understanding and exploiting behavior that is associated with the chaotic regions to identify useful trajectory arcs. The CRP model is frequently suitable to yield first-order mission design solutions, but useful information is frequently difficult to isolate amidst the chaos. Investigation of Lagrangian coherent structures in the CRP supplies additional insight.

### III.III The Bicircular Four-body Model

The bicircular four-body problem incorporates the influence of a fourth body as a perturbation to the restricted problem dynamics. The relative geometry of such a system is depicted in Fig. 2, where an initial angle for the fourth body with respect to the CRP rotating  $x$ -axis is denoted  $\theta_0$ . Under this model, a

<sup>§</sup>CRP and “restricted problem” are used interchangeably here, both refer to the circular restricted three-body problem.

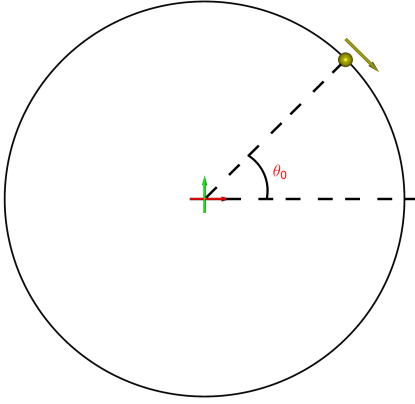


**Fig. 2: The Bicircular Four-body Problem**

fourth distant gravitating body is placed on a circular orbit relative to the barycenter of the CRP. Consequently, the Newtonian inverse-square gravity of the fourth body acts on the spacecraft in addition to the gravitational effects of the two CRP primaries. The fourth body does not effect the circular Keplerian orbits of the two “local” bodies. In this case, the Sun is added as the fourth body orbiting the Earth–Moon barycenter on a circular orbit at a distance of 1 AU. The equations of motion remain the same as Equations [6a]–[6c], but the potential function is now,<sup>24</sup>

$$U^* = \frac{1 - \mu}{r_{13}} + \frac{\mu}{r_{23}} + \frac{\mu_4}{r_{43}} + \frac{1}{2}(x^2 + y^2), \quad [8]$$

with  $\mu_4 = \frac{m_4}{m_1 + m_2}$ .

Such a four-body model, while still reflecting significant simplification, introduces an important transition. The presence of the perturbing fourth body results in a non-autonomous system. This change in the nature of the system decreases the applicability of many of the dynamical systems tools that are available in the CRP, while completely removing others. A constant of the motion, and, consequently, a convenient expression for bounds on the motion, is no longer available. Other aspects of the problem now shift with time (e.g., manifolds still exist, in a sense, but are no longer invariant). These evolving structures are useful to illustrate the extensibility and usefulness FTLE/LCS analysis.

### III.IV A Four-body Ephemeris Model

A partial ephemeris model is employed and is selected as an incremental increase in fidelity from the bicircular model, much like the bicircular model offered an incremental step beyond the restricted problem. These small modifications in models are engineered to highlight the changes resulting from various contributions to the fidelity of the model. This higher-fidelity, four-body ephemeris model is similar to that employed by Pavlak and Howell,<sup>25</sup> a Moon–Earth–Sun (MES) point mass model with position histories supplied by JPL DE405 ephemerides. The present model, in contrast

to Pavlak and Howell, does not include Solar radiation pressure. The governing equations are the  $n$ -body relative equations of motion,

$$\ddot{\bar{r}}_{q3} = -\frac{\mu_{2b,3} + \mu_{2b,q}}{r_{q3}^3} \bar{r}_{q3} + \sum_{\substack{j=1 \\ j \neq 3,q}}^n \mu_{2b,j} \left( \frac{\bar{r}_{3j}}{r_{3j}^3} - \frac{\bar{r}_{qj}}{r_{qj}^3} \right). \quad [9]$$

Here,  $\mu_{2b} = Gm$ , consistent with the 2BP. The position vector,  $\bar{r}_{qj}$ , indicates the position of the  $j^{\text{th}}$  body with respect to the central body,  $q$ ; the subscript 3 is associated with the spacecraft. In this model, states defined in the restricted problem are transitioned to Moon-centered J2000 states via an instantaneous rotating frame defined by ephemerides.

This partial ephemeris model naturally involves full six-dimensional states and trajectory propagation is performed in all spatial dimensions. Additionally, computation of the FTLE employs auxiliary “grid” points about each state variable. Thus, in this model, one FTLE computation involves the propagation of 12 perturbations. Notwithstanding these spatial considerations, since the maps are transitioned from the planar lower-fidelity model, their domain remains the same.

These models illustrate the wide applicability of FTLE/LCS analysis to different types of systems. Ultimately, this extensibility indicates that this type of metric and mapping strategy can be employed for a full-ephemeris design and analysis. Such capability is supported by previous FTLE literature in other fields which describes the FTLE as a tool for directly analyzing empirical flow results (when no underlying dynamical model is defined).<sup>6,12</sup>

## IV. MAPS

Mapping analysis within the context of multi-body regimes has proven to effectively reveal design options that are otherwise difficult to identify (see, for example, Davis and Howell<sup>26</sup>). Some advantages of a map based approach include a broader view of the design space as well as a “cleaner” visual that offers easier categorization of the behavior in a specific region. The maps employed in this analysis share many aspects with well-known mapping strategies. A key difference is the quantity visualized with the mapping. Specifically, these maps focus on FTLE values across an area in contrast to the returns to a hyperplane in a traditional Poincaré plot. Another difference is the Lagrangian perspective that is inherent in calculating the FTLE. Traditional maps depict the evolution of the trajectories in terms of their crossings on the map. A map of FTLE is essentially a map reflecting the fates of each trajectory evolving from a set of initial conditions where the focus of the investigation is the stretching downstream at some future time. Several possible mapping strategies are described below.

## IV.I State–space Maps

Investigations of many systems involve a traditional Poincaré mapping to create a puncture plot that facilitates analysis. Such a map reveals salient information by reducing the dimension of the system and alleviating obscuration. Elements of this Poincaré mapping approach are employed, including the selection of a hyperplane corresponding to some value of a single state variable; a grid is constructed from two other state variables; and, the fourth state is constrained by a system integral. However, rather than creating a return map, the initial grid coordinates (representing an entire state in the planar CRP) are colored by relative FTLE value. Thus, each of the initial states is characterized.

While there are many possible representations available for observing the behavior in a system, strategies frequently involve the investigation of position–velocity phase spaces. For example, a map can be plotted in terms of a position variable and its associated velocity component. Alternatively, a “mixed” position–velocity phase space (i.e., a position and the alternate velocity component in a four–dimensional state), or quantities derived from combinations of the state also prove useful as mapping coordinates. In the state spaces associated with the models in this analysis, a true Poincaré mapping constructed from both a hyperplane and a constant of the motion, as described previously, is not always available. However, establishing the initial conditions associated with a particular mapping in one model and then adjusting these states for application to the other models is a possibility. For ease of contrast and comparison between various maps, this analysis includes both position–velocity and position–position Poincaré maps. Specifically, in the CRP, one state variable is assigned a particular value to define the hyperplane, two other state variables are selected on a grid and the fourth is supplied by the Jacobi constant. The initial conditions associated with such a map are then adjusted for use in the higher–fidelity models through state transformations.

## IV.II Apse Maps

One particular type of map can be constructed using a condition of the state, rather than sampling a state variable, to define the hyperplane. Passage through closest approach or maximal excursion is employed to construct an apse map. The periapse or apoapse condition indicates a hyperplane crossing. Two state variables again serve as the map domain. Both the apse conditions and the Jacobi constant are enforced to recover the remaining two state variables. Such an apse map can be displayed in terms of various state variable combinations, but position variables are particularly useful as a more intuitive mapping. An application of this type of map is described by Haapala<sup>27</sup> and Howell et al.<sup>28</sup> among others. FTLE maps defined in spe-

cific regions correlate closely with manifold Poincaré apse maps constructed by a direct mapping of the invariant manifolds. These FTLE maps highlight similar structures and reveal additional information due to their dense nature.<sup>18</sup> An example of this type of map showcasing repelling and attracting manifold structures near the smaller primary in the Sun–Saturn system appears in Fig. 3. In Fig. 3, red structures

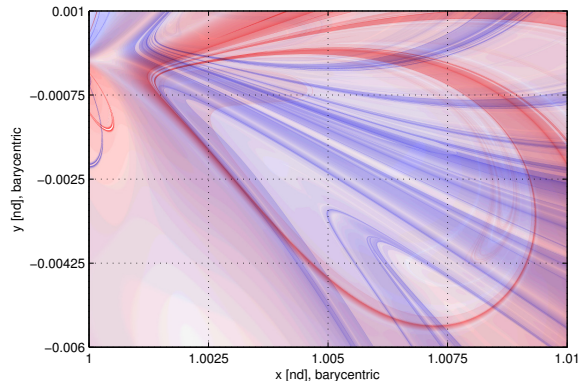


**Fig. 3: A Sun–Saturn  $P_2$  Periapse FTLE Map**

reflect high values of backward FTLE and the corresponding ridges<sup>¶</sup> do, in fact, correlate to the periapse passages of  $L_1$  unstable manifold trajectories. Similarly, blue structures are associated with the stable manifold periapses. Apse maps are useful to the study of transit orbits as described by Haapala.<sup>27</sup>

## IV.III Stroboscopic Maps

Traditional stroboscopic maps are constructed as Poincaré maps with a hyperplane condition selected as a particular time, for example, the characteristic period of a system. Alternatively, this time condition may be arbitrarily defined. Crossings in this type of map are recorded every  $T$  time units, where  $T$  is the time condition defined for the hyperplane. Such a stroboscopic map may be more insightful with repeating behavior. A common application of FTLE maps that is consistent with the definition of Lagrangian coherent structures is, effectively, a single iteration of a stroboscopic map. That is, LCS are defined as structures emerging when the flow map is evaluated at the same final time,  $T$ , for all initial states. This type of map highlights the stretching of nearby trajectories at a specified later time and allows for more direct comparison across an entire field of FTLE values.

One essential value of the finite–time Lyapunov exponent for predicting behavior is captured by examining large groupings of FTLE values in a region. This approach leads directly to creating maps of FTLE values. Aspects from the various types of mapping strategies can be combined to effectively illustrate the

<sup>¶</sup>While LCS are defined as ridges of FTLE, this is not entirely accurate in the case of a periapse map where iterations occur at different times along each trajectory.

flow in an astrodynamical model. The information that emerges from these maps can then be incorporated into different phases of mission design and analysis.

## V. DESIGN AND ANALYSIS

Maps of the finite-time Lyapunov exponent and the associated structures that emerge are effective in support of trajectory design activities. Since the LCS revealed in CRP FTLE maps are analogous to invariant manifolds, existing manifold-based design strategies directly apply. In more complex scenarios involving more than two gravity fields, invariant manifold structures are no longer available. However, in such regimes, time-evolving barriers still exist. For a given reference time, these flow-separating structures can be exploited in much the same way as the invariant manifolds in the CRP. The following examples highlight some of the uses of FTLE maps and the associated LCS.

### V.I LEO to the Map: 2BP

Transfers from LEO to the neighborhood of the cis-lunar ( $L_1$ ) libration point involving manifold and “pseudo-manifold” arcs in the Earth-Moon system serve as specific examples of LCS applications. Many recent missions have involved revolutions in the vicinity of the libration points for phasing or other considerations. The objective of this example is to identify transfers from FTLE/LCS maps that result in a successful revolution about  $L_1$  (indicating a potential for insertion into an orbit about  $L_1$ ). A Hohmann-type transfer arc from LEO to the vicinity of the stable branch of a  $L_1$  Lyapunov orbit manifold-crossing with the  $y$ -axis in the CRP rotating frame is employed to establish this particular scenario. The CRP energy level is selected to be consistent with an  $L_1$  gateway that is slightly open (as defined by the zero-velocity curves), and an  $L_2$  gateway that is closed.

The Hohmann transfer in this example is selected simply to result in a final state to compare with initial conditions in a scenario that illuminates the insight available from an FTLE mapping. The transfer arc is a two-body arc that departs a 300 km altitude low Earth orbit at perigee for a maneuver cost of slightly less than  $3 \frac{\text{km}}{\text{s}}$ . The arc is constructed to specifically reach apogee at the  $y$ -axis crossing in a rotating frame consistent with the CRP (i.e.,  $x = 0$ ). The LEO parking orbit (yellow) and the Hohmann arc are illustrated in Fig. 4. In Fig. 4, the magenta and blue arcs represent the inertial and rotating views of the Hohmann arc, respectively. The green and red axes are the  $y$ -axis and  $x$ -axis of the barycentric rotating frame. The rotating frame and the inertial frame are aligned such that the two frames overlap when the Hohmann arc reaches  $x = 0$  as viewed by a rotating observer. Both arcs are included to illustrate a scenario such that a

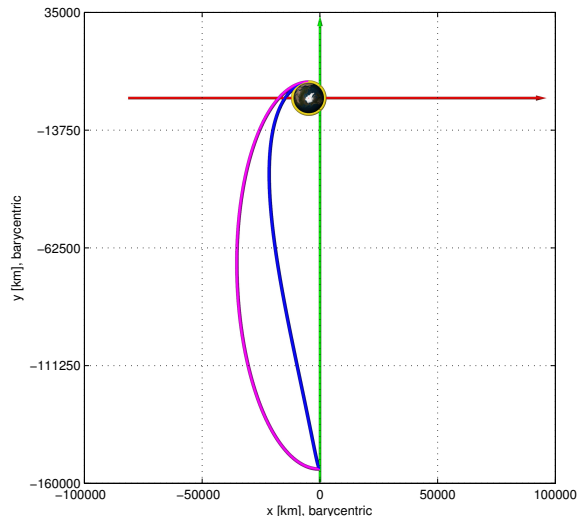
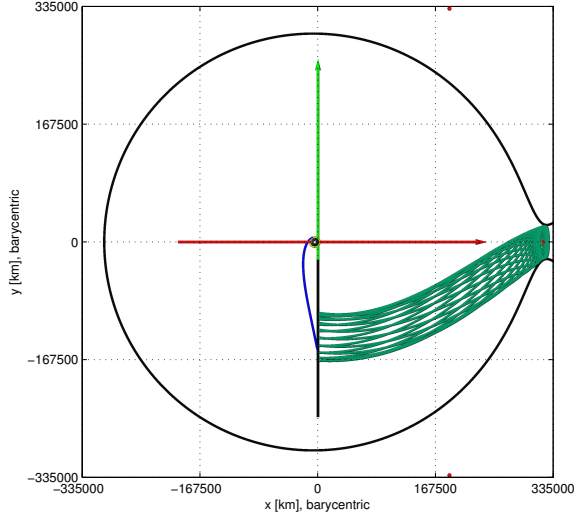


Fig. 4: Arcs from LEO to Region of Interest:  $x = 0$  (Magenta: Inertial, Blue: Rotating)

spacecraft might be delivered to a region where manifold structures are known to exist in the CRP. Thus, the arc is computed using only simple two-body conic analysis—this type of arc could be targeted in the restricted problem, but for its purpose here, it is not necessary. The arc allows for a simple estimate of maneuver cost to depart LEO, and based on the resulting state at the manifold insertion point (i.e., at the  $x = 0$  crossing, in this case) an estimate for a maneuver cost to insert onto a manifold structure.

### V.II From the Map to $L_1$ : CRP

Selection of an energy level in the CRP, consistent with an open  $L_1$  gateway and an  $L_2$  gateway that is closed, enables the computation of a periodic Lyapunov orbit about  $L_1$  and the associated invariant manifolds. For the purposes of illustrating the map employed in this example, the  $P_1$  branch of the stable manifold is depicted in configuration space in Fig. 5. The surface of section selected for this example ranges from approximately  $-250,000$  km to  $-20,000$  km along the rotating  $y$ -axis and is colored black in Fig. 5. Also included in the figure, for perspective, are the interior ZVC for this energy level (black contour) as well as the  $L_1$ ,  $L_4$  and  $L_5$  libration points represented as the upper, middle and lower red spheres, respectively. The transfer arc also appears in the rotating frame. The section for this analysis is selected such that  $x = 0$ ,  $(-250112 < y < -19239)$  km,  $(-0.9733 < \dot{y} < 0.5635) \frac{\text{km}}{\text{s}}$  and  $\dot{x}$  is recovered from  $C = C_{L_2}$ . However, many of the visuals are zoomed to  $(-192,394 < y < -76,957.2)$  km,  $(-0.5891 < \dot{y} < 0.1793) \frac{\text{km}}{\text{s}}$ , to focus on the structures of interest. Introducing the appropriate initial conditions, and allowing them to evolve forward in time for 3.5 nondimensional (nd) time steps ( $\sim 15.198$  days) yields FTLE values consistent with Fig. 6. Central to Fig. 6 is a curve of relatively higher FTLE values along



**Fig. 5:**  $P_1$  Stable Manifold Branch for  $C = C_{L_2}$

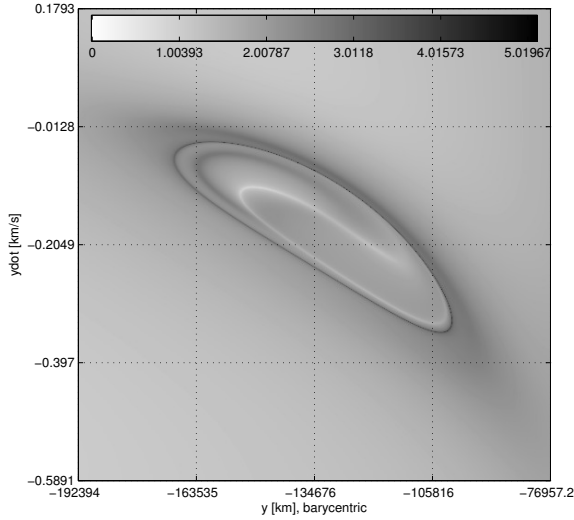


**Fig. 6:** FTLE for  $C = C_{L_2}$  in the CRP

its edge. In this figure, as well as others, the FTLE value is indicated by the color bar near the top of the image. This contour is a Lagrangian coherent structure that corresponds to the interior, or  $P_1$ , branch of the stable manifold that flows into the Lyapunov orbit near  $L_1$ .

The state along the Hohmann arc as it crosses  $x = 0$  is projected onto the map from Fig. 6. While the  $x$ ,  $y$  and  $\dot{y}$  components lie on the map, the  $\dot{x}$  component from the arc is not constrained. From the position of the projected state on the map, it is observed that velocity adjustments in both components allow for insertion into two possible manifold trajectories. These two potential insertion points lie on the map where the transfer arcs possess the same  $y$  value as the manifold contour. These various options appear in Fig. 7. The state marked in blue represents the projection of the Hohmann arc state on the map. Of the two insertion possibilities on the contour with the same  $y$  value, the lower  $\dot{y}$  option is selected as indicated by the black

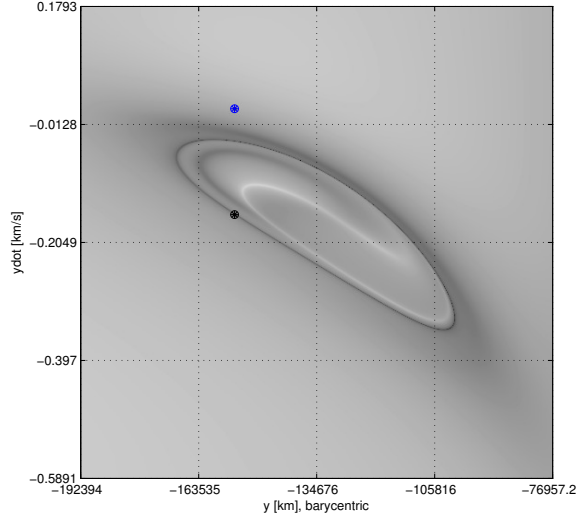


**Fig. 7:** Hohmann Projection & Selected Manifold

marking. The two-body Hohmann arc allows for a rough estimate of the maneuver cost to insert onto the manifold arc in the restricted problem. In this scenario, the cost is computed by,

$$|\Delta v| \approx \sqrt{(v_{x,m} - v_{x,h})^2 + (v_{y,m} - v_{y,h})^2} \quad [10]$$

or,

$$\begin{aligned} |\Delta v| &\approx 1.373 \frac{\text{km}}{\text{s}} \\ &= \sqrt{(1.823 - 0.451)^2 + (-0.147 - 0.014)^2} \end{aligned}$$

where subscripts  $,m$  and  $,h$  correspond to the manifold and Hohmann arc components, respectively. This maneuver cost, coupled with the LEO departure maneuver cost, (together  $\approx (1.4 + 3.0)$ ), is reasonable given (1) the assumptions in this problem, and (2) the consideration that there is no attempt to determine an optimal solution.

The state selected from the map serves only as an approximation for the associated manifold trajectory since the resolution of the map is significantly larger than the precision required for actual manifold trajectories. Nevertheless, a very slight adjustment to the map state yields manifold-like results. In Figs. 8 and 9, two trajectories selected from the map are plotted along with a state reflecting minimal adjusting of the velocity “by hand”. The two grid points that bound the adjusted state correspond to  $\dot{y} \approx -0.1546$  nd (trajectory enters  $P_2$  region) and  $\dot{y} \approx -0.1561$  nd (trajectory does not enter  $P_2$  region). Selecting  $\dot{y} = -0.155$  produces the black trajectory with the desired behavior, that is a revolution about  $L_1$  resembling a Lyapunov orbit as is apparent in Fig. 9.

Since the map resolution is relatively large (as compared to the level of accuracy for manifold states), some correction is necessary to generate a more optimal value for an insertion velocity state. However, in

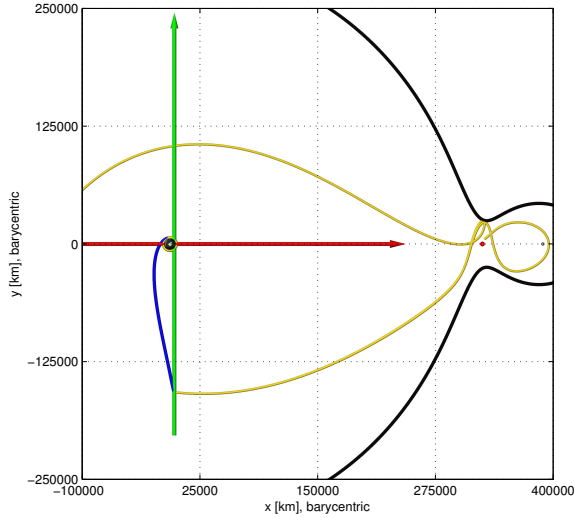


**Fig. 8: Two Trajectories from Map States**

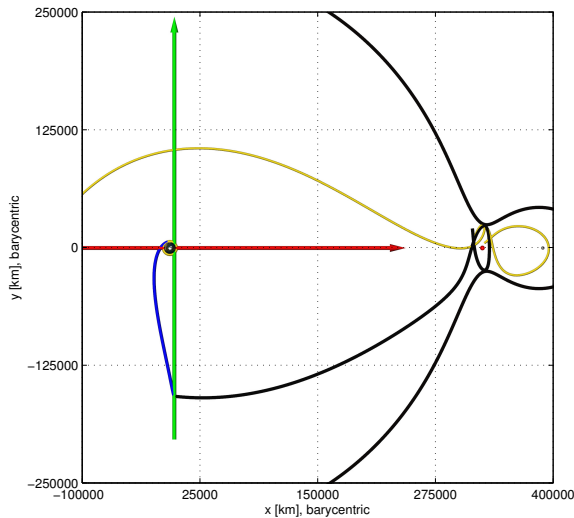


**Fig. 9: Manually Adjusted Trajectory**

general, the map supplies a very good initial guess for the manifold. This insight is less critical in the CRP since alternate schemes/approaches are available to directly produce the manifolds. In contrast, for more complex models, the manifold-like structures are more obscure and information from the map is very useful.

### V.III From the Map to $L_1$ : 4BP

The power of FTLE analysis lies in the ability to describe the flow in complex models. Transitioning the initial states associated with the map in the CRP into the bicircular four-body problem represents a first step towards using FTLE in a higher-fidelity astrodynamical context. Introducing the perturbing effect of the Sun's gravity on the CRP dynamics renders the resulting system non-autonomous. To demonstrate the applicability of the same FTLE tools, several maps are generated with varying initial Sun angles with respect to the Earth-Moon rotating frame. From the

rotating frame perspective, the Sun revolves entirely about the Earth-Moon system in one synodic period of the Moon. Thus, the perturbation resulting from the addition of the Sun's gravity periodically repeats. Moreover, the Solar gravity effects on the trajectory arc for some initial angular offset reflect across the origin. For example, an initial offset of  $0.25\pi$  radians for the Sun's position with respect to the rotating  $x$ -axis will induce results that are similar to those that emerge if the initial offset is  $1.25\pi$  radians. Thus, selecting initial offsets between  $0$  and  $\pi$  radians is sufficient for preliminary analysis. Considering the time frame in this example,  $\sim 15.198$  days, or roughly half of the synodic Earth-Moon period, a number of initial Sun angles should reveal different structures. For extended time frames in this model, on the order of months, the perturbations, effectively, average out. In Figs. 10–12, different initial Sun angles morph the LCS in an FTLE map. For ease of comparison, differences are highlighted in Fig. 13.

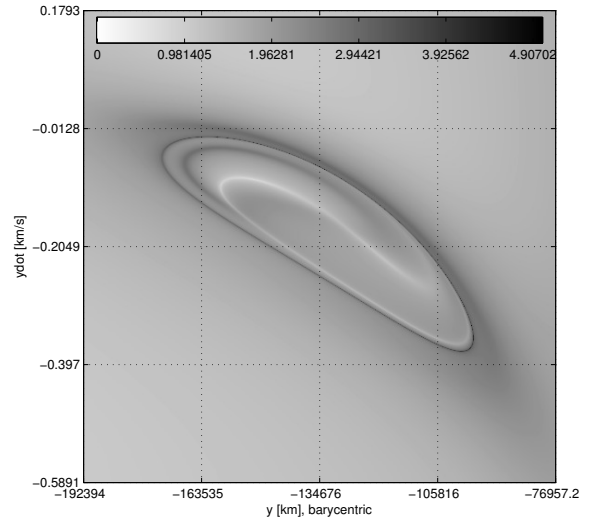


**Fig. 10: Initial Sun Angle:  $0.25\pi$**

In an assessment of the bicircular four-body problem, over timescales of about 15 days, the Solar gravity does little to alter the structure qualitatively. However, to a small degree, the structures shrink, grow, or translate along the “long-axis” of the lobe described by the LCS, depending on the initial Solar angle. While these modifications are slight, they are significant since an initial state close to the manifold in the CRP would move further away from the corresponding structure in the 4BP. More precisely, the structures are shifted between the two models. This displacement depends on the initial location of the Sun, and changes as the LCS evolves in time.

Comparison between the structures that appear under the CRP versus the 4BP, suggests an idea of the type of adjustment required, based on the initial Sun angle, to place the state on the four-body “manifold”. Depicted in Fig. 14, the difference between the CRP

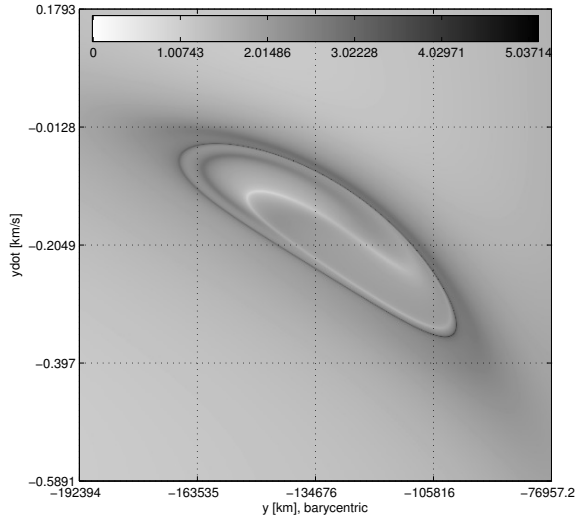


Fig. 11: Initial Sun Angle:  $0.50\pi$

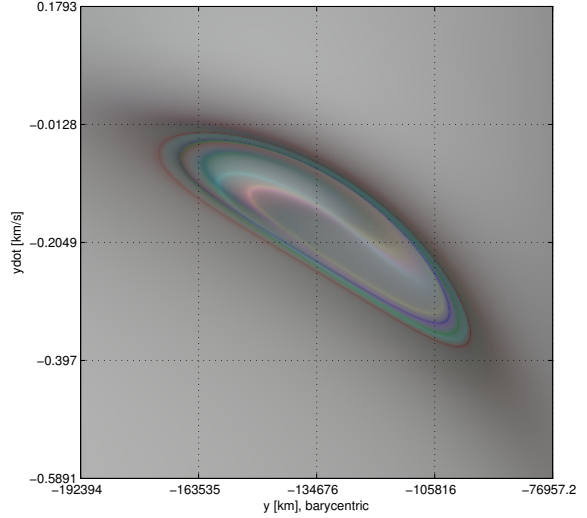


Fig. 13:  $0.25\pi$  (red),  $0.50\pi$  (green),  $0.75\pi$  (blue)

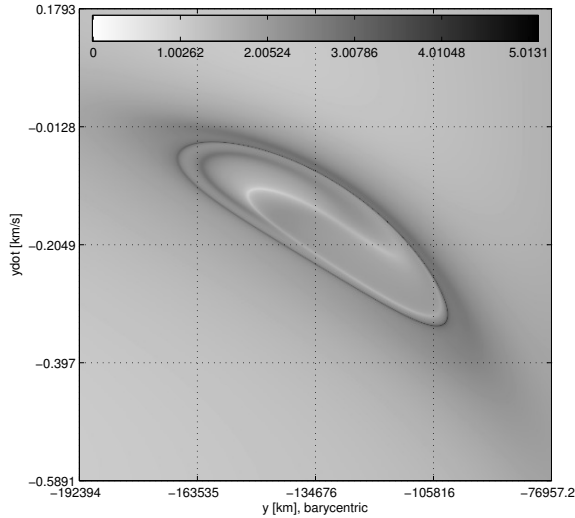


Fig. 12: Initial Sun Angle:  $0.75\pi$

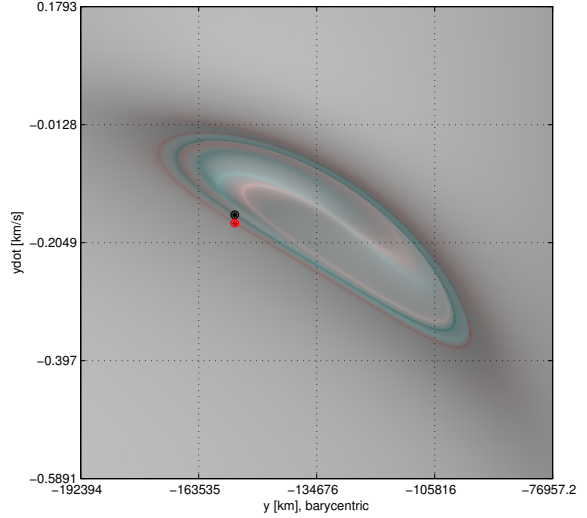


Fig. 14: CRP (green) vs.  $0.25\pi$  4BP (red)

map in Fig. 6 and the  $0.25\pi$  4BP map is apparent. The red contour is the LCS from the 4BP while the green contour is the structure from the CRP map. Propagating the initial conditions associated with the state marked in black in Fig. 14 (i.e., the black trajectory from Fig. 9) in the 4BP results in a trajectory that enters the  $P_2$  region as illustrated by the red colored trajectory in Fig. 15. The CRP arc is included, again in black, for comparison. Finally, selecting an alternative state directly from the map, a four-dimensional state that lies near the 4BP contour (this time marked in red in Fig. 14) produces the red manifold-like trajectory in Fig. 16. Again the CRP arc generated from the same state is plotted for comparison in black.

The comparison between structures in the restricted problem and the bicircular problem demonstrates the use of a procedure for applying FTLE/LCS concepts in different models. The ability to visually identify structure in the 4BP is encouraging since the structures themselves are not as readily calculable from

the traditional methods applied to generate manifolds in the autonomous CRP. Additionally, in both cases, the flow behavior is characterized through the relatively simple computation of FTLE values, although many such calculations are required. While the computational overhead to produce large grids of FTLE is not trivial, it can be offset by adaptive methods and parallelization. Investigation of FTLE maps and the underlying structures in the bicircular model provides an incremental step towards applying the tools in even more complex models and assists in establishing and verifying the conceptual progression between models. Further analysis in a higher-fidelity model solidifies the applicability of these methods in practical scenarios.

#### V.IV From the Map to $L_1$ : MES

Transition to an ephemeris model, even as in the Moon–Earth–Sun model, immediately introduces several new considerations. The previous models were

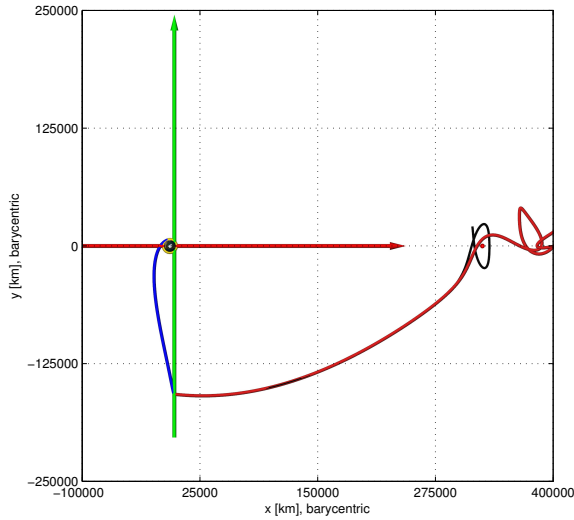


**Fig. 15: CRP State Evolved in 4BP**

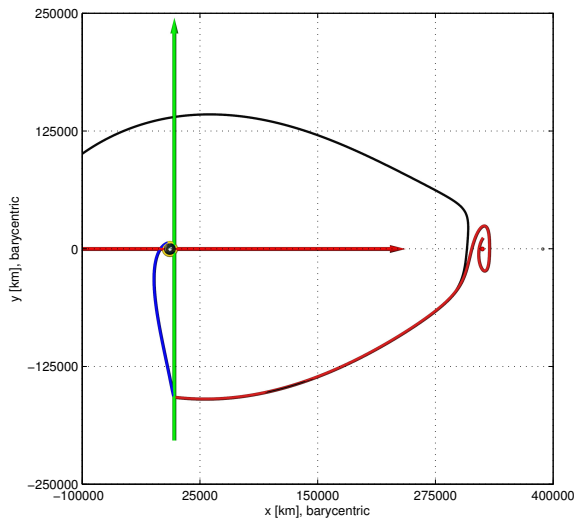


**Fig. 16: 4BP Manifold Arc**

developed in a planar four-dimensional state space. Since Solar System bodies move in all three spatial dimensions, the trajectories integrated to evaluate the FTLE must also be evolved spatially (i.e., in all 6 dimensions of the state space). Fortunately, the formulation of the FTLE still applies directly since the value of interest, the eigenvalue associated with the direction of largest expansion, can still be calculated. Thus, transitioning from CRP to J2000 states for a particular epoch supplies initial conditions that are directly integrated using the relative equations of motion defined in Equation [9]. Moreover, neighboring states integrated forward or backward in time still expand and contract with the flow as dictated by the dynamics. Thus, representing the FTLE on the same map space continues to apply. The process begins by transitioning a CRP state, and ends with the resulting FTLE value and the appropriate “coloring” of the initial state on the map. The structures in the map are now expected to shift for each different initial epoch. In Fig. 17, maps of FTLE

values are represented on the same section that was employed in the previous maps, but zoomed out to the full extent. The epochs associated with the maps in the sequence progress down the first column and then down the second column. Initial dates for integrating the field were selected about August 1, 2012 at 00:00:00 UTC. Thus, referencing from the upper left corner of the figure, the initial epochs range from July 27 through August 5 in the bottom right corner (all starting at 00:00:00 UTC). The lower left corner in each frame of

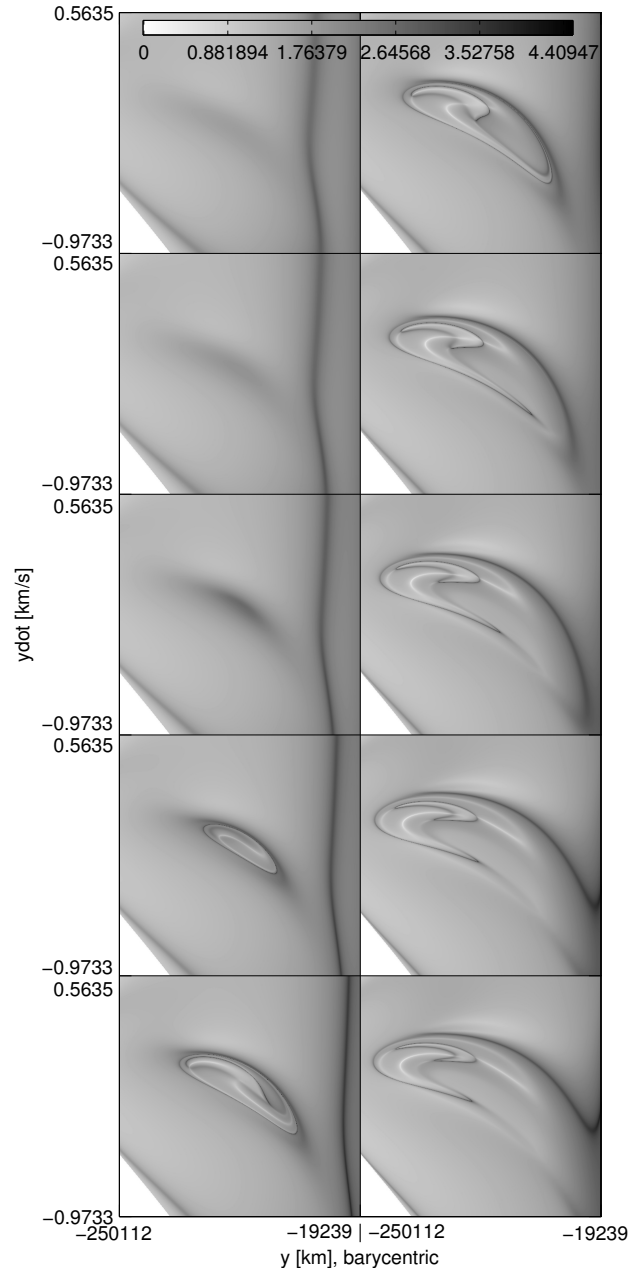
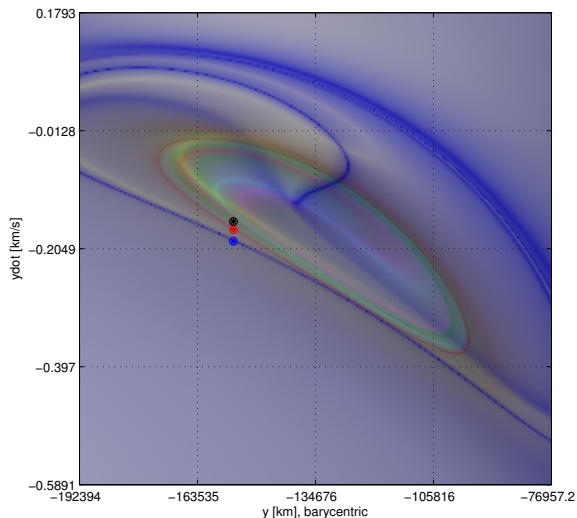


**Fig. 17: July 27 – August 5 Ephemeris FTLE**

the figure reflects a region beyond the CRP zero velocity curves in  $y-\dot{y}$  space. Thus, this region is empty of FTLE values.

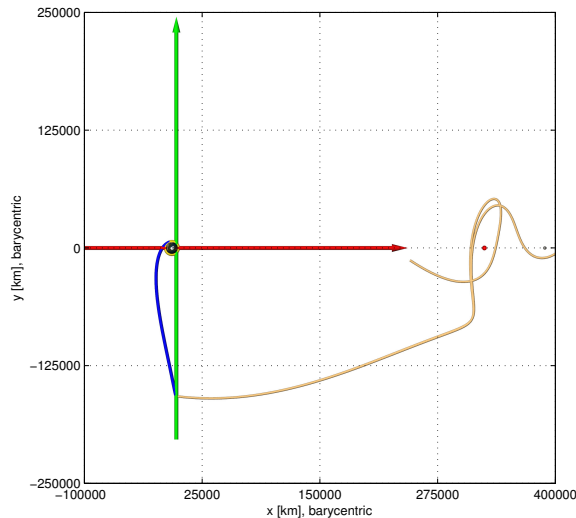
As is apparent from the ephemeris sequence in

Fig. 17, there are some dates for which the structures of interest do not appear and others for which the structures no longer form closed contours on the map. Comparing the map for a selected ephemeris epoch with the maps constructed in the CRP and the 4BP illustrates the similarities to the maps developed in the previous models. The view in Fig. 18 is consistent with the map in the restricted problem for  $C = C_{L_2}$ , and with the map in the bicircular problem for an initial Solar offset of  $0.25\pi$ , as well as the resulting ephemeris map for the epoch August 1, 2012 at 00:00:00 UTC. The CRP structures appear in green and the 4BP structures are colored red. The new ephemeris map information appears in blue—the blue levels have been slightly exaggerated for clarity. The position and velocity states of interest are again marked with different colors. As before, the state corresponding to the trajectory from the model for the restricted problem is marked in black and the state associated with the 4BP trajectory is marked red. The state employed in the subsequent ephemeris propagation appears as well, with a blue marking. Taking state vectors directly from the grid



**Fig. 18: FTLE Maps for CRP  $C_{L_2}$  (green), 4BP  $\theta_0 = 0.25\pi$  (red), MES Aug. 1, 2012 (blue)**

near the ephemeris structure and evolving them forward in time produces the tan arcs depicted in Fig. 19. The arc that continues towards  $P_2$  results from an initial state with  $\dot{y} \approx -0.1868$  nd, while the arc that revolves about  $L_1$  and presumably returns to the  $P_1$  region originates from a state with  $\dot{y} \approx -0.1883$  nd. Next, in Fig. 20, a manually adjusted trajectory with initial  $\dot{y} = -0.18809$  appears colored in blue. As was observed when transitioning from the restricted problem to the bicircular problem, the maps from the ephemeris propagations and the associated LCS offer good estimates for (1) the locations for the likely existence of potentially useful, or (2) the existence of any, manifold-like arcs for particular conditions. Moreover, the ephemeris maps supply predictive information that



**Fig. 19: Two Ephemeris Trajectories from the Map**

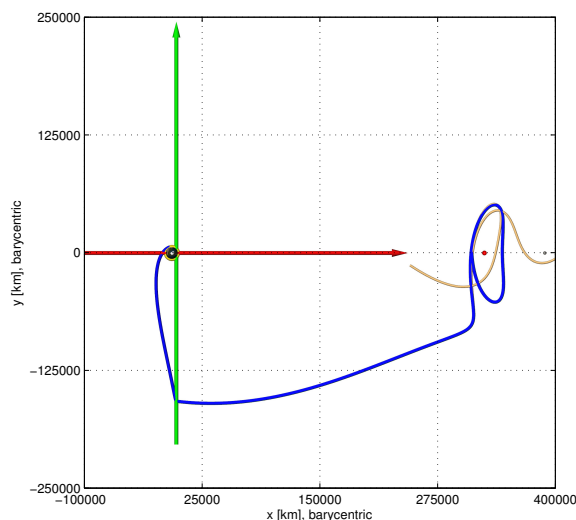


**Fig. 20: Manually Adjusted Ephemeris Trajectory**

is valuable in a design scenario. The fact that, for a given CRP energy level, ephemeris “manifolds” may not exist for a particular epoch, or that these structures may possess a significantly different qualitative nature is useful. Maps of FTLE values yield significant insight in complex models.

Comparing maps of FTLE across different models supplies significant insight into the flow similarities and differences under the models. Additionally, such a comparison highlights the magnitude of various effects. In the bicircular problem, it is apparent that the gravitational perturbation from the Sun over timescales consistent with this analysis, while significant, does little to alter the qualitative nature of the structures appearing in FTLE maps. In scenarios where non-planar, non-Keplerian gravitational sources are present, it is apparent that the initial epoch can impact the dynamical structure significantly. These types of comparisons can offer dynamical context for design and yield more understanding of the nature of the flow.

## V.V A Brief Ephemeris Analysis Example

The FTLE/LCS concepts can not only add insight for design, but also support analysis. Recent ARTEMIS trajectory phases involved significant operations in the vicinity of the Earth–Moon  $L_1$  and  $L_2$  libration points. Effective stationkeeping during these phases was important for mission success. The computation of FTLE values adds some context for the ARTEMIS maneuver strategy. Previous analysis by Folta et al.,<sup>29</sup> as well as Pavlak and Howell,<sup>30</sup> demonstrates that the optimal, plane–constrained stationkeeping maneuvers during the Lyapunov phases of the ARTEMIS trajectory correlate strongly with the stable direction recovered from an approximate monodromy matrix ( $M$ ) associated with revolutions of the trajectory. The optimal maneuver direction for a stationkeeping cycle aligns with the position projection of the stable eigenvector computed from an approximation to the monodromy matrix. These results are consistent with the FTLE values in the vicinity of a single maneuver point.

To explore one stationkeeping maneuver consider a reconstruction of one revolution along the path of the ARTEMIS  $P1$  spacecraft (not to be confused with the major primary in the CRP). Specifically, the focus is one revolution about  $L_2$  in the Earth–Moon system as depicted in Fig. 21. The red horizontal line is the

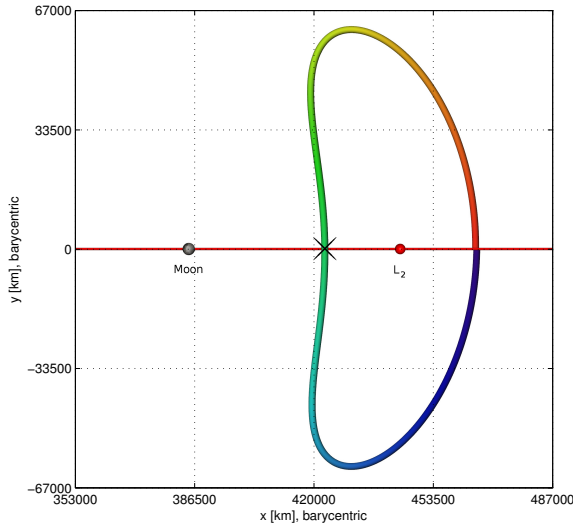


Fig. 21: Uncorrected Artemis  $P1$ ,  $L_2$  Segment

rotating  $x$ -axis, the red sphere,  $L_2$ , and the Moon is depicted to scale. The actual spacecraft implemented a maneuver near the  $x$ -axis between the Moon and  $L_2$ , as marked with the black  $\times$  in the figure, on November 17, 2010 08:45:00 UTC. The direction of motion along this arc is denoted with color; it begins in violet and terminates in red. Thus the trajectory is recovered by evolving forward in time (1.80 nd time steps,  $\sim 7.86$  days) from the maneuver point as well as propagating backward in time (1.90 nd time steps,  $\sim 8.29$  days). To serve as a basis for comparison, the uncor-

rected ARTEMIS  $P1$  state is evolved in an ephemeris system similar to the one described in Section III.IV—the same system employed in the FTLE ephemeris map construction. However, for this example, the central body is the Earth, thus, the system is denoted an Earth–Moon–Sun (EMS) system. Despite the planar representation of the trajectory in Fig. 21, it does experience significant out-of-plane excursions during the plotted stationkeeping cycle.

To generate the stable and unstable directions from an approximate monodromy matrix for the arc shown in Fig. 21, finite differences are used to generate both the forward and backward state transition matrices (STM  $\Phi$ ). These STM are combined by multiplying the inverse of the backward STM and the forward STM, that is,

$$M = (\Phi(t_0, t_{-1}))^{-1} \Phi(t_1, t_0) \quad [11]$$

where  $t_{-1}$  corresponds to the originating point (violet) on the trajectory arc and  $t_1$  is the time of the final state. The time,  $t_0$ , is the maneuver time. For the purposes here, the maneuver is not actually implemented, rather, its direction is compared with (1) the stable direction as computed from  $M$ , and (2) surrounding FTLE values. The directions of the relevant vectors and the FTLE values at various points in the surrounding field appear in Figs. 22–25. Three orthographic projections as well as a 3D view are included in the figures.

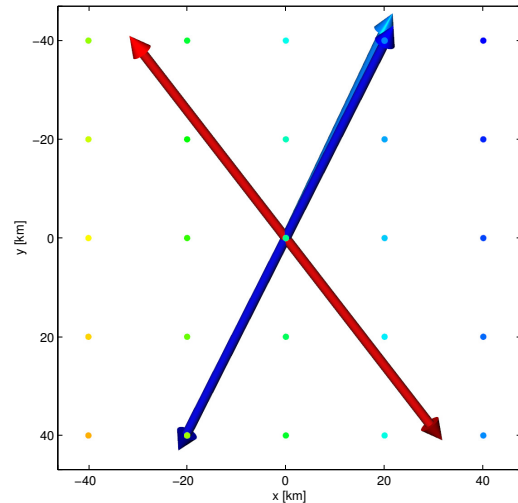


Fig. 22: Maneuver and Stability Directions ( $x$ - $y$ )

In the figures,  $x$ - $y$ - $z$  Cartesian axes appear; in the 3D view in Fig. 25 the axes are colored in darker shades of red, green and blue, respectively. In each of the figures, the stable eigen-directions from the monodromy matrix are represented by double-headed blue arrows, while the unstable eigen-directions are depicted as double-headed red arrows. The direction of the actual ARTEMIS  $P1$  maneuver is indicated in the figures as the cyan arrow. Each of the directions are scaled in length for clarity. Also plotted in the figures are points

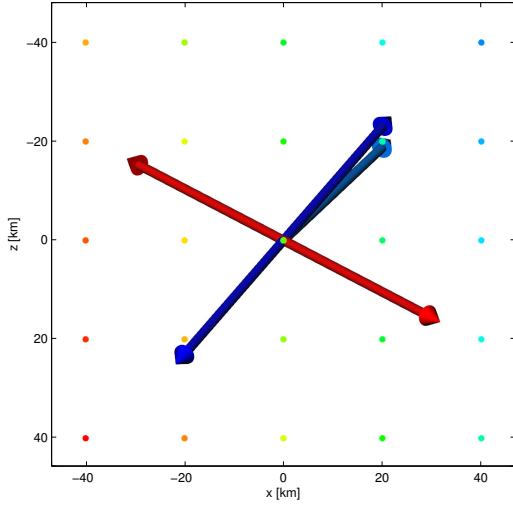


Fig. 23: Maneuver and Stability Directions ( $x-z$ )

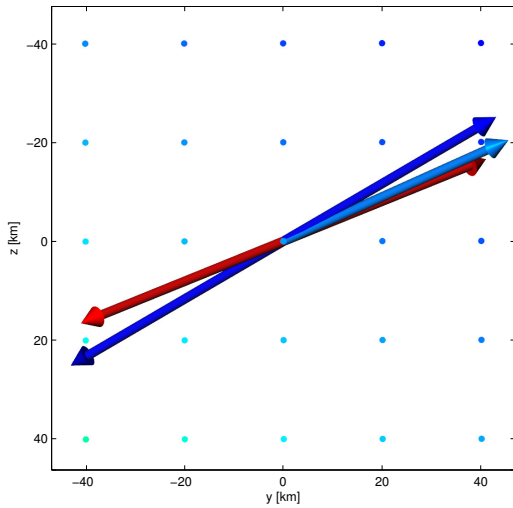


Fig. 24: Maneuver and Stability Directions ( $y-z$ )

of forward time FTLE values colored using a “rainbow” color-scale with red denoting the largest magnitude of the values of forward FTLE and blue coloring the lowest values. In the planar figures, the relative FTLE coloring is taken from the top-most slice, for a given projection, on the boundary of the cube (as seen in Fig. 25). These FTLE values are generated by stepping away from the maneuver position in steps of 20 km to form a  $5 \times 5 \times 5$  point grid of FTLE values spanning a cube of  $\pm 40$  km. Each grid point is evolved forward for a time consistent with the forward propagation of the arc in Fig. 21. Thus, a three-dimensional stroboscopic map of FTLE results. Similar cubes of backward FTLE as well as both forward and backward FTLE generated by perturbing velocity states are consistent with the forward FTLE values depicted in Figs. 22–25. Observe that the actual maneuver direction aligns well with the stable direction as described by Folta et al. as well as Pavlak and Howell. Additionally, the optimal maneuver is directed generally in the least sensitive direction (the direction of the blue points) as illustrated by the

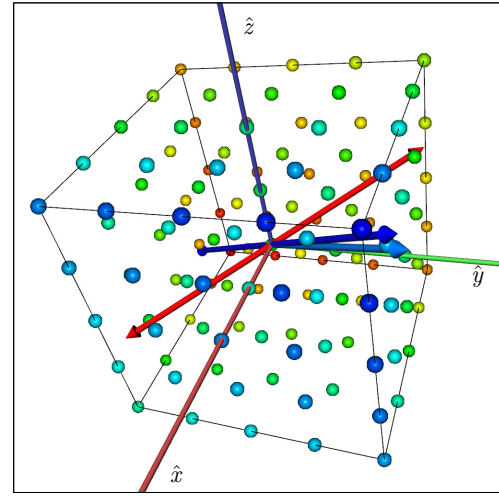


Fig. 25: Maneuver and Stability Directions (3D)

3D FTLE grid. That is, the maneuver direction, orients toward smaller FTLE values consistent with the stable direction.

The brief analysis of an ARTEMIS maneuver from an FTLE perspective simply serves to illustrate the metric’s usefulness in analysis. While this example evaluates only a single maneuver, additional investigation of FTLE values and optimal maneuvers from the ARTEMIS mission is ongoing. Both the design and analysis examples in this section serve to describe the effectiveness of the FTLE and associated LCS as investigative tools.

## VI. CONCLUSIONS AND FUTURE WORK

The examples offer possible FTLE/LCS-based types of analysis. Maps of FTLE values characterize the overall flow in a system and reveal manifold and manifold-like structures. Additionally, information revealed from FTLE values adds some details concerning local stability. The general qualitative nature of FTLE maps supplies useful contextual information and general insight. Moreover, the potential exists for utilizing relative FTLE values in corrections algorithms.

Additional investigation is warranted into the applications of FTLE/LCS tools within astrodynamical contexts. Specifically, in light of the ARTEMIS associated example, more work towards FTLE analysis about mission maneuvers would help to validate its effectiveness for this type of application. Preliminary results seem to indicate that maneuver directions may be most optimal in the direction of least sensitivity (as determined by neighboring FTLE) along the stable eigen-direction of the monodromy matrix.

Further study of comparative maps should continue to prove useful. Additional maps in ephemeris spaces will help to identify other structures and aid in mission design. Taking advantage of emerging parallelization hardware and software, will lead to real-time imple-

mentation of FTLE maps in the design process. Many useful avenues of investigation for FTLE/LCS based analysis in astrodynamics remain to be studied.

## VII. ACKNOWLEDGEMENTS

The authors wish to thank Daniel Pérez Palau and Professor Gerard Gómez of the University of Barcelona for assistance towards additional refinement of the algorithms employed in many of the computations as well as general insight and perspective into the work. Thanks to Tom Pavlak for information on the ARTEMIS mission and ephemeris models. Thanks are also due to Professors Xavier Tricoche and George Haller for additional input on various aspects of the work. This work was conducted at Purdue University. Partial support was provided by assistantships from the Schools of Aeronautics and Astronautics and Engineering Education as well as the Rune and Barbara Eliassen Aerospace Visualization Laboratory.

## REFERENCES

- <sup>1</sup>G. Haller, "Finding finite-time invariant manifolds in two-dimensional velocity fields," *Chaos*, vol. 10, no. 1, pp. 99–108, 2000.
- <sup>2</sup>G. Haller, "Distinguished material surfaces and coherent structures in three-dimensional fluid flows," *Physica D*, vol. 149, pp. 248–277, 2001.
- <sup>3</sup>G. Haller and G. Yuan, "Lagrangian coherent structures and mixing in two-dimensional turbulence," *Physica D*, vol. 147, pp. 352–370, 2000.
- <sup>4</sup>G. Haller, "Lagrangian coherent structures from approximate velocity data," *Physics of Fluids*, vol. 14, no. 6, pp. 1851–1861, 2002.
- <sup>5</sup>S. C. Shadden, F. Lekien, and J. E. Marsden, "Definition and properties of Lagrangian coherent structures from finite-time Lyapunov exponents in two-dimensional aperiodic flows," *Physica D*, vol. 212, pp. 271–304, 2005.
- <sup>6</sup>M. Mathur, G. Haller, T. Peacock, J. Ruppert-Felsot, and H. Swinney, "Uncovering the Lagrangian Skeleton of Turbulence," *Physical Review Letters*, vol. 98, pp. 144502–1–4, 2007.
- <sup>7</sup>F. Lekien, S. C. Shadden, and J. E. Marsden, "Lagrangian coherent structures in n-dimensional systems," *Journal of Mathematical Physics*, vol. 48, pp. 065404–1–19, 2007.
- <sup>8</sup>G. Haller, "A variational theory of hyperbolic Lagrangian Coherent Structures," *Physica D*, vol. 240, pp. 574–598, 2011.
- <sup>9</sup>M. Farazmand and G. Haller, "Computing Lagrangian Coherent Structures from Variational LCS theory," *Chaos*, vol. 22, no. 013128, 2012.
- <sup>10</sup>G. Haller and F. J. Beron-Vera, "Geodesic theory of transport barriers in two-dimensional flows," *Physica D*, 2012. in press, preprint available at [http://georgehaller.com/reprints/geodesic\\_theory\\_of\\_transport\\_barriers.pdf](http://georgehaller.com/reprints/geodesic_theory_of_transport_barriers.pdf).
- <sup>11</sup>C. Garth, F. Gerhardt, X. Tricoche, and H. Hagen, "Efficient Computation and Visualization of Coherent Structures in Fluid Flow Applications," *IEEE Transactions on Visualization and Computer Graphics*, vol. 13(6), pp. 1464–1471, 2007.
- <sup>12</sup>T. Peacock and J. Dabiri, "Introduction to focus issue: Lagrangian coherent structures," *Chaos*, vol. 20, pp. 017501–1–3, 2010.
- <sup>13</sup>R. L. Anderson, M. W. Lo, and G. H. Born, "Application of Local Lyapunov Exponents to Maneuver Design and Navigation in the Three-Body Problem," in *AAS/AIAA Astrodynamics Specialist Conference*, (Big Sky, Montana), August 3-7, 2003. Paper No. AAS 03-569.
- <sup>14</sup>M. Lara, R. P. Russell, and B. Villac, "Classification of the Distant Stability Regions at Europa," *Journal of Guidance, Control, and Dynamics*, vol. 30, no. 2, pp. 409–418, 2007.
- <sup>15</sup>B. F. Villac, "Using FLI maps for preliminary spacecraft trajectory design in multi-body environments," *Celestial Mechanics and Dynamical Astronomy*, vol. 102, no. 1-3, pp. 29–48, 2008.
- <sup>16</sup>B. Villac and S. Broschart, "Applications of Chaoticity Indicators to Stability Analysis Around Small Bodies," in *19<sup>th</sup> AAS/AIAA Space Flight Mechanics Meeting*, (Savannah, Georgia), February 9-12, 2009. Paper No. AAS 09-221.
- <sup>17</sup>E. S. Gawlik, J. E. Marsden, P. C. du Toit, and S. Campagnola, "Lagrangian coherent structures in the planar elliptic restricted three-body problem," *Celestial Mechanics and Dynamical Astronomy*, vol. 103, no. 3, pp. 227–249, 2009.
- <sup>18</sup>C. Short, K. Howell, and X. Tricoche, "Lagrangian Coherent Structures in the Restricted Three-Body Problem," in *21<sup>st</sup> AAS/AIAA Space Flight Mechanics Meeting*, (New Orleans, Louisiana), 2011. Paper No. AAS 11-250.
- <sup>19</sup>D. Pérez, G. Gómez, and J. J. Masdemont, "Detecting Invariant Manifolds Using Hyperbolic Lagrangian Coherent Structures," in *1st IAA/AAS Conference on the Dynamics and Control of Space Systems*, (Porto, Portugal), March 19-21, 2012.
- <sup>20</sup>G. Haller and T. Sapsis, "Lagrangian Coherent Structures and the Smallest Finite-Time Lyapunov Exponent," *Chaos*, vol. 21, no. 023115, pp. 1–7, 2011.
- <sup>21</sup>D. Eberly, R. Gardner, B. Morse, and S. Pizer, "Ridges for Image Analysis," *Journal of Mathematical Imaging and Vision*, vol. 4, pp. 355–371, 1994.
- <sup>22</sup>F. Diacu, "The Solution of the  $n$ -body Problem," *The Mathematical Intelligencer*, vol. 18, no. 3, pp. 66–70, 1996.
- <sup>23</sup>V. Szebehely, *Theory of Orbits: The Restricted Problem of Three Bodies*. New York: Academic Press, 1967.
- <sup>24</sup>J. J. Guzman, *Spacecraft Trajectory Design in the Context of a Coherent Restricted Four-Body Problem*. PhD thesis, Purdue University, West Lafayette, Indiana, 2001.
- <sup>25</sup>T. Pavlak and K. Howell, "Evolution of the Out-of-Plane Amplitude for Quasi-Periodic Trajectories in the Earth-Moon System," in *IAF 62<sup>nd</sup> International Astronautical Conference*, (Cape Town, South Africa), October 2011.
- <sup>26</sup>D. C. Davis and K. C. Howell, "Characterization of Trajectories Near the Smaller Primary in the Restricted Problem for Applications," *Journal of Guidance, Control, and Dynamics*, vol. 35(1), pp. 116–128, 2012.
- <sup>27</sup>A. F. Haapala, "Trajectory Design Using Periapse Maps and Invariant Manifolds," Master's thesis, School of Aeronautics and Astronautics, Purdue University, West Lafayette, Indiana, 2010.
- <sup>28</sup>K. C. Howell, D. C. Davis, and A. F. Haapala, "Application of Periapse Maps for the Design of Trajectories Near the Smaller Primary in Multi-Body Regimes," *Journal of Mathematics Problems in Engineering, Special Issue: Mathematical Methods Applied to the Celestial Mechanics of Artificial Satellites*, vol. 2012, Article ID 351759.
- <sup>29</sup>D. Folta, M. Woodard, and D. Cosgrove, "Stationkeeping of Lissajous Trajectories in the Earth-Moon System with Applications to ARTEMIS," in *20<sup>th</sup> AAS/AIAA Astrodynamics Specialist Conference*, (Girdwood, Alaska), March 31-August 4, 2011. Paper No. AAS 11-515.
- <sup>30</sup>T. A. Pavlak and K. C. Howell, "Strategy for Optimal, Long-Term Stationkeeping of Libration Point Orbits in the Earth-Moon System," in *AIAA/AAS Astrodynamics Specialist Conference*, (Minneapolis, Minnesota), August 2012.